Journal of Inorganic Biochemistry 278 (2026) 113234

Contents lists available at ScienceDirect

Journal of Inorganic Biochemistry

journal homepage: www.elsevier.com/locate/jinorgbio

Synthesis, structural characterization, and antitumor evaluation of Pd(II) Thiosemicarbazide–Diphosphine complexes in 2D and 3D cancer models ☆

Dario B. Fortaleza [a,*], Josias S. Rocha [a], George B.S. Pereira [a], Tamara Teixeira [a], Jocely L. Dutra [a], Carlos A.F. Moraes [a], Pedro H.O. Santiago [b], Alzir A. Batista [a], Moacir R. Forim [a], Javier A. Ellena [b], Fillipe V. Rocha [a,*]

[a] Departamento de Química, Universidade Federal de São Carlos – UFSCar, CP 676, 13561-901 São Carlos, SP, Brazil
[b] Instituto de Física de São Carlos, Universidade de São Paulo – USP, CP 369, 13560-970 São Carlos, SP, Brazil

ARTICLE INFO

Keywords:
Cancer
Antitumor
Pd(II)
Thiosemicarbazide
3D cell culture

ABSTRACT

Cancer remains one of the leading causes of death worldwide, with millions of new cases diagnosed annually. Cisplatin is a major advance in chemotherapy, but its severe side effects and the development of resistance limit its long-term effectiveness. In this context, palladium(II) complexes have gained attention as structural analogues of platinum compounds because they have the potential to exhibit antitumor activity while reducing toxicity. Six novel palladium(II) complexes containing thiosemicarbazide derivatives and diphosphine ligands [1,3-bis (diphenylphosphine)propane (dppp) or 1,4-bis(diphenylphosphine)butane (dppb)] were synthesized and thoroughly characterized by FTIR, ^{1}H NMR and ^{31}P NMR, high-resolution mass spectrometry, UV–Vis spectroscopy, and single-crystal X-ray diffraction. The structural analyses confirmed distorted square-planar Pd(II) geometries featuring N,S-bidentate thiosemicarbazide and chelating bisphosphine ligands. The cytotoxicity of the complexes was evaluated against breast (MCF-7 and MDA-MB-231), prostate (DU-145), lung (A549), ovarian (A2780 and A2780cis), and non-tumor (MRC-5) cell lines using MTT (3-(4,5-dimethylthiazol-2-yl)-2,5-diphenyltetrazolium bromide) assays. One of the complexes exhibited the highest cytotoxicity, with IC_{50} values approaching 1 μM in ovarian and breast cancer cells. B3 was about 25–30 times more active and selective than cisplatin (SI ≈ 15). Additional tests demonstrated that B3 blocked colony formation and migration, triggered dose-dependent apoptosis, and exhibited minimal toxicity to non-tumor cells. Notably, B3 demonstrated significant activity against cisplatin-resistant ovarian cells (A2780cis) in three-dimensional (3D) spheroid cultures, indicating its potential under physiologically relevant conditions. Overall, the structural features represent a promising lead compound for developing next-generation palladium-based metallodrugs with improved selectivity and effectiveness against resistant tumor types.

1. Introduction

Cancer comprises more than a hundred distinct diseases characterized by uncontrolled cell proliferation and impaired programmed cell death mechanisms [1–3]. Unregulated growth of malignant cells leads to primary tumor formation, which can metastasize through the circulatory and lymphatic systems, establishing secondary tumors that are often the most aggressive and life-threatening forms of the disease [4,5].

According to Global Cancer Statistics 2022, there were approximately 20 million new cancer cases and 9.7 million deaths worldwide. The most prevalent cancers are lung (12.4%), breast (11.6%), colorectal (9.6%), prostate (7.3%), and stomach (4.9%) cancers, and demographic projections suggest that the global incidence may reach 35 million new cases annually by 2050 [6].

The serendipitous discovery of cisplatin's antitumor properties by Rosenberg and colleagues in 1968, followed by its FDA approval in 1978, marked a milestone in the development of metal-based chemotherapeutics. Cisplatin is still a cornerstone drug with broad efficacy against ovarian, breast, testicular, lung, bladder, head and neck cancers. However, its lack of selectivity toward malignant cells results in severe, dose-limiting toxicities, including nephrotoxicity, neurotoxicity, ototoxicity, and myelosuppression [7–9].

☆ This article is part of a Special issue entitled: 'Baran Special Issue' published in Journal of Inorganic Biochemistry.

* Corresponding authors.
E-mail addresses: dario.fortaleza@estudante.ufscar.br (D.B. Fortaleza), fillipe@ufscar.br (F.V. Rocha).

https://doi.org/10.1016/j.jinorgbio.2026.113234
Received 11 November 2025; Received in revised form 26 December 2025; Accepted 14 January 2026
Available online 21 January 2026

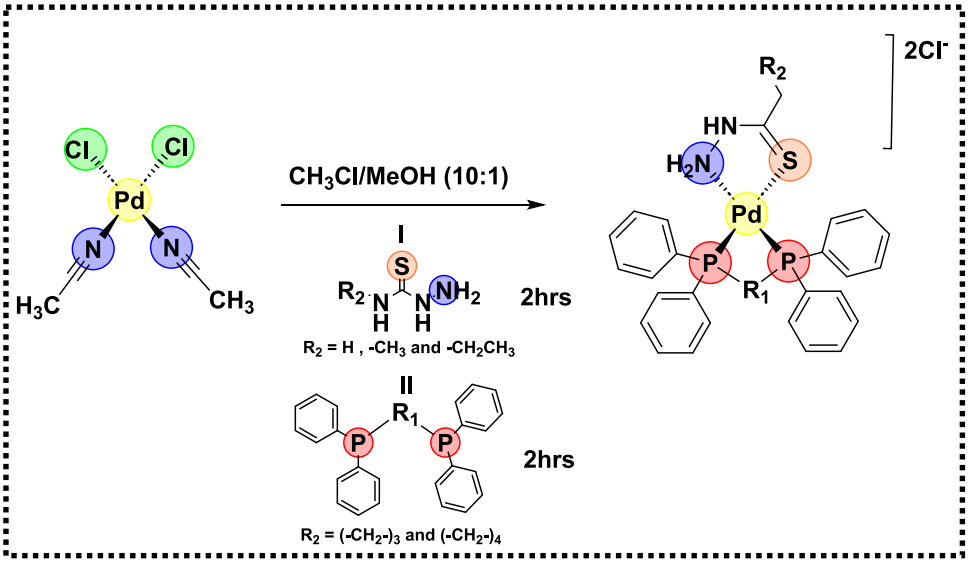

Scheme 1. Synthesis of Palladium complexes.

Efforts to mitigate these adverse effects have led to the development of second- and third-generation platinum drugs, such as carboplatin and oxaliplatin, that have improved pharmacological profiles [10,11]. In parallel, the therapeutic landscape has been expanded by exploring alternative transition metals. Among these metals, palladium is a promising candidate due to its close chemical similarity to platinum [12,13]. However, Pd(II) species generally exhibit faster ligand-exchange kinetics, requiring the use of chelating or bulky ligands to enhance structural stability. Palladium(II) complexes bearing donor atoms, such as nitrogen, sulfur, and phosphorus, have shown notable cytotoxic activity. Thiosemicarbazide and phosphine ligands are particularly promising scaffolds in this regard [14–16].

Thiosemicarbazides are versatile ligands that can stabilize metal centers through N,S-bidentate coordination. They are also known to exhibit a wide range of biological activities, including antibacterial, antifungal, anti-inflammatory, antioxidant, antiviral, and antitumor effects [17–20]. Phosphine ligands, in turn, enhance lipophilicity and cellular permeability upon metal coordination. This is exemplified by the potent antineoplastic activity of gold(I) phosphine complexes [21–23].

Developing more predictive biological models is critical for discovering selective anticancer agents. Although widely used, conventional two-dimensional (2D) cell cultures fail to reproduce the complexity of the tumor microenvironment. Three-dimensional (3D) culture systems, such as multicellular tumor spheroids, better mimic physiological conditions by incorporating nutrient and oxygen gradients, cell-to-cell interactions, and differential proliferation zones [24–26]. Consequently, 3D models improve the translational relevance of preclinical assays, enabling the early identification of compounds with genuine therapeutic potential and reducing reliance on animal testing [27,28].

In this context, the present study describes the synthesis and characterization of six new palladium(II) complexes that contain thiosemicarbazide derivatives (TSC = Thiosemicarbazide; MeTSC = 4-Methylthiosemicarbazide; EtTSC = 4-Ethylthiosemicarbazide) either 1,3-bis(diphenylphosphine)propane (dppp) or 1,4-bis(diphenylphosphine)butane (dppb) ligands. The complexes' antitumor properties were investigated using a panel of human cancer and non-tumor cell lines. Then, mechanistic and 3D spheroid assays were performed on the most active compound. This integrated approach provides new insights into the structure-activity relationships of Pd(II) thiosemicarbazide-diphosphine complexes as potential anticancer agents.

2. Materials and methods

2.1. Physicochemical measurements

Infrared (IR) spectra were recorded on a Shimadzu IRTracer-100 spectrometer in the 4000–220 cm^{-1} range using CsI pellets prepared at a 100:1 (CsI:sample) mass ratio, averaging 64 scans per spectrum. ^{1}H and ^{31}P NMR spectra were acquired in deuterated methanol (MeOD) on a Bruker AVANCE III 9.4 T spectrometer. Molar conductivity measurements were performed using a Meter Labs CDM230 conductivity meter with 1.0×10^{-3} mol L^{-1} solutions in DMSO. High-resolution mass spectra (HRMS) were obtained on an Agilent 6545 qTOF MS (Agilent Technologies, Santa Clara, CA, USA) equipped with an electrospray ionization (ESI) source operating in positive-ion mode. Single-crystal X-ray diffraction data were collected on an XtaLAB Synergy Dualflex HyPix diffractometer at 100.00(13) K. using Cu Kα (1.54184 Å) radiation. The structure was solved by the *Intrinsic Phasing* method using ShelXT [29] and refined by full-matrix least-squares minimization on F^2 with ShelXL 2019/2. The program Olex2 [30] was used as a graphical interface. The structure of B3 was refined using the solvent mask (Bypass) option of Olex2, which indicated the presence of two chloride ions and 1.2 molecules of chloroform per asymmetric unit. The CIF files of B1 and B3 were deposited in the Cambridge Structural Database with CCDC numbers 2,492,316 and 2,492,317, respectively.

2.2. Synthesis of complexes

2.2.1. General method

The precursor *cis*-$[PdCl_2(CH_3CN)_2]$ was synthesized according to a previously reported procedure [31]. The palladium precursor (0.20 mmol) was dissolved in 22 mL of a $CHCl_3$/MeOH (10:1, *v*/v) mixture under magnetic stirring. Subsequently, the corresponding thiosemicarbazide derivative (TSC, MetTSC or EtTSC, 0.20 mmol) was added, and the reaction mixture was stirred for 2 h at room temperature. The immediate formation of a colorless precipitate was observed, consistent with the coordination of the thiosemicarbazide derivatives to Pd(II). Subsequently, dppp or dppb (0.20 mmol) was added, and the reaction mixture was stirred for an additional 2 h. Upon addition of the diphosphine ligand, the initially formed colorless solid gradually dissolved, giving rise to a homogeneous yellow solution, indicative of successful coordination of the diphosphine to the metal center (Scheme 1). The resulting mixture was filtered by gravity and concentrated by rotary evaporation to approximately 2 mL. The product was precipitated

by the addition of diethyl ether or n-hexane (15 mL), collected by vacuum filtration, and dried in a desiccator under reduced pressure.

2.2.2. [Pd(dppp)(TSC)]Cl_2 (P1)

^{1}H NMR (400 MHz, MeOD): δ 7.92–7.47 (m, 20H), 3.08–3.00 (m, 4H), 2.34–2.23 (m, 2H). ^{31}P{^{1}H} NMR (162 MHz, MeOD): δ 9.29–8.70 (d, $J_{p\text{-}p}$ = 43.1 Hz), 3.28–2.70 (d, $J_{p\text{-}p}$ = 41.8 Hz). IR (CsI, cm^{-1}): 3600–3205 ν(NH2), 3194–3039 ν(C-H)sp^2, 2927 ν(CH)sp^3, 1631 δ(NH), 1232 ν(C=S), 1436, 1099, 748, 694 e 509 (PPh_2). UV–vis (MeOH): λmáx 287 nm (Ɛ = 13,979.464 $Lmol^{-1}$ cm^{-1}); ESI-MS: (*m/z*) [M - H]$^+$: 608.0670 (calc), 608.0686 (exp). Yield of 88.6%.

2.2.3. [Pd(dppp)(4-MeTSC)]Cl_2 (P2)

^{1}H NMR (400 MHz, MeOD) δ 7.72–7.48 (m, 20H), 3.12–3.01 (m, 4H), 2.81 (s, 3H), 2.35–2.23 (m, 2H). ^{31}P{^{1}H} NMR (162 MHz, MeOD) δ 9.40–8.46 (d, $J_{p\text{-}p}$ = 42.8 Hz), 3.70–2.75 (d, $J_{p\text{-}p}$ = 43.3 Hz). IR (CsI, cm^{-1}): 3658 ν(N-H), 3452 e 3331 ν(NH2 e NH), 3153, 3053 e 3012 ν(C-H)sp^2, 2931, 2899 e 2800 ν(CH)sp^3, 1627 δ(NH), (1571) ν(C═C e C═N), 1232 ν(C=S), 1436, 1103, 750, 698 e 511 (PPh_2). UV–vis (MeOH): λ_{max} 287 nm (Ɛ = 13,632.692 $Lmol^{-1}$ cm^{-1}); ESI-MS: (*m/z*) [M - H]$^+$: 622.0822 (calc) 622.0838 (exp),; [M]$^{2+}$: 311.5447 (calc) 311.5458 (exp). Yield of 74.25%.

2.2.4. [Pd(dppp)(4-EtTSC)]Cl_2 (P3)

^{1}H NMR (400 MHz, MeOD) δ 7.74–7.44 (m, 20H), 3.29–3.05 (s, 4H), 3.05–2.93 (m, 2H), 2.83–2.72 (s, 1H), 2.39–2.18 (m, 2H), 1.22–1.08 (m, 3H). ^{31}P{^{1}H} NMR (162 MHz, MeOD) δ 9.43–8.70 (d, J = 42.6 Hz), 3.74–2.70 (d, $J_{p\text{-}p}$ = 47.3 Hz). IR (CsI, cm^{-1}): 3600–3300 ν(N-H), 3051 ν(C-H)sp^2, 2985, 2931 ν(CH)sp^3, 1627 δ(NH), 1571 ν(C═C e C═N), 1435, 1101, 748, 692 e 513 (PPh_2). UV–vis (MeOH): λ_{max} 283 nm (Ɛ = 13,681.731 $Lmol^{-1}$ cm^{-1}). ESI-MS: (*m/z*) [M - H]$^+$: 636.0978 (calc) 636.0992 (exp); [M]$^{2+}$: 318.5525 (calc) 318.5539 (exp). Yield of 84.97%.

2.2.5. [Pd(dppb)(TSC)]Cl_2 (B1)

^{1}H NMR (400 MHz, MeOD) δ 7.85–7.45 (m, 20H), 3.15–3.04 (t, J = 9.0 Hz, 2H), 2.60–2.44 (m, 4H), 1.93–1.79 (d, J = 23.6 Hz, 2H). ^{31}P{^{1}H} RMN (162 MHz, MeOD) δ 31.18–30.50 (d, $J_{p\text{-}p}$ = 34.6 Hz), 19.48–18.80 (d, $J_{p\text{-}p}$ = 34.4 Hz). IR (CsI, cm^{-1}): 3630–3200 ν(NH_2), 3194–3039 ν(C-H)sp^2, 2983–2920 ν(CH)sp^3, 1633 δ(NH), 1236 ν(C=S), 1435, 1099, 744, 696 e 501 (PPh_2). UV–vis (MeOH): λ_{max} 291 nm (Ɛ = 12,021.429 $Lmol^{-1}$ cm^{-1}); 255 nm (Ɛ = 15,208.929 $Lmol^{-1}$ cm^{-1}). ESI-MS: (*m/z*) [M-H+]: 622.0822 (calc) 622.0843 (exp). Yield of 90.01%.

2.2.6. [Pd(dppb)(4-MeTSC)]Cl_2 (B2)

^{1}H NMR (400 MHz, MeOD) δ 7.75–7.61 (ddt, J = 13.9, 12.5, 4.4 Hz, 12H), 7.61–7.51 (qd, J = 7.9, 2.7 Hz, 8H), 3.25–3.08 (m, 2H), 2.93–2.78 (s, 3H), 2.63–2.55 (t, J = 5.4 Hz, 1H), 2.55–2.46 (q, J = 5.8 Hz, 3H), 1.95–1.76 (d, J = 22.9 Hz, 2H). ^{31}P{^{1}H} RMN (162 MHz, MeOD) δ 31.60–30.97 (d, $J_{p\text{-}p}$ = 34.9 Hz), δ 19.15–18.52 (d, $J_{p\text{-}p}$ = 34.6 Hz). IR (CsI cm^{-1}): 1043597–3300 ν(N-H), 3180, 3051 (C-H) sp^2, 2935 ν(CH) sp^3, 1631 δ(NH), (1570) ν(C═C e C═N), 1436, 1099, 746, 696 e 526 (PPh_2). UV–vis (MeOH): λ_{max} 291 nm (Ɛ = 13,142.308 $Lmol^{-1}$ cm^{-1}); 255 nm (Ɛ = 18,242.308 Lmol-1 cm-1). ESI-MS: (*m/z*) [M - H]$^+$: 636.0978 (calc) 636.1000 (exp); [M]$^{2+}$: 318.5525 (calc) 318.5538 (exp). Yield of 89%.

2.2.7. [Pd(dppb)(4-EtTSC)]Cl_2 (B3)

^{1}H NMR (400 MHz, MeOD) δ 7.74–7.51 (m, 20H), 3.22–3.08 (m, 3H), 2.64–2.45 (d, J = 31.6 Hz, 4H), 1.92–1.78 (m, 2H), 1.22–1.11 (t, J = 7.4 Hz, 3H). ^{31}P{^{1}H} NMR (162 MHz, MeOD) δ 31.69–30.93 (d, $J_{p\text{-}p}$ = 35.8 Hz), 19.03–18.26 (d, $J_{p\text{-}p}$ = 35.3 Hz). IR (CsI cm^{-1}): 3600–3309 ν(N-H), 3174, 3051 (C-H) sp^2, 2978 e 2935 ν(CH)sp^3, 1627 δ(NH), 1570 ν(C═C e C═N), 1436 1192, 1099, 746, 696, 528 (PPh_2). UV–vis (MeOH): λ_{max} 290 nm (Ɛ = 12,342 $Lmol^{-1}$ cm^{-1}); 259 nm (Ɛ = 21,777 $Lmol^{-1}$ cm^{-1}). ESIMS: (*m/z*) [M - H]$^+$: 650.1135 (calc) 650,1136 (exp), (m/z) [M] $^{2+}$: 325.5604 (calc) 325.5616 (exp). Yield of 70%.

2.3. Biological assays

2.3.1. Cell culture conditions

For the biological assays, the following human cell lines were used: triple-negative breast tumor MDA-MB-231 (ATCC HTB-26), breast tumor MCF-7 (ATCC HTB-22), lung tumor A549 (ATCC CCL-185), prostate tumor DU-145 (ATCC HTB-81), ovarian tumor A2780 (ECACC 93112519), cisplatin-resistant ovarian tumor A2780cis (ECACC 93112517), and non-tumor lung fibroblast MRC-5 (ATCC CCL-171). The MDA-MB-231, A549, DU-145, and MRC-5 cell lines were maintained in DMEM (Dulbecco's Modified Eagle Medium; Vitrocell) supplemented with 10% fetal bovine serum (FBS), whereas MCF-7, A2780, and A2780cis cells were cultured in RPMI-1640 medium (Roswell Park Memorial Institute; Vitrocell) containing 10% FBS. All cell lines were grown at 37 °C in a humidified incubator with 5% CO_2.

2.3.2. Cell viability assay

Cell viability was evaluated using the MTT (3-(4,5-dimethylthiazol-2-yl)-2,5-diphenyltetrazolium bromide) assay. Cells were seeded at a density of 1.5 × 10^4 cells per well in 150 µL of supplemented culture medium in 96-well plates. After incubating for 24 h at 37 °C and 5% CO_2, the cells were treated with test compounds dissolved in DMSO at various concentrations (0.8, 1.6, 3.1, 6.3, 12.5, 25, 50, and 100 µM). The plates were then incubated for an additional 48 h under the same conditions. After incubation, 50 µL of MTT solution (1 mg/mL) was added to each well. The plates were incubated for an additional 4 h, after which the medium was carefully removed and 100 µL of isopropanol was added to dissolve the resulting formazan crystals. Absorbance was measured at 540 nm using an Epoch microplate reader (BioTek Instruments, USA). IC_{50} values were calculated using GraphPad Prism 8.0.2 software. All experiments were performed in triplicate.

2.3.3. Colony formation assay

Cells from the A2780cis, MDA-MB-231, and MRC-5 lines were seeded in 6-well plates at a density of 1.0 × 10^3 cells per well in 2 mL of culture medium supplemented with 10% fetal bovine serum (FBS) and maintained in a humidified incubator at 37 °C with 5% CO_2 for 24 h. After cell adhesion, the cells were treated with *v*arious concentrations of complex B3 (0.25, 0.51, 1.01, 2.02, and 4.04 µM) and incubated for 48 h. A control group received DMSO (0.5%) under the same conditions. Following treatment, the medium was replaced with fresh drug-free medium, and the plates were incubated for 10 days to allow colony formation. After this period, the cells were washed with PBS, fixed with a methanol:acetic acid (3:1, *v*/v) solution for 5 min, and stained with 5% crystal violet for 30 min. The number of colonies was quantified using ImageJ software. All experiments were performed in triplicate.

2.3.4. Cell morphology analysis

Cells from the A2780cis, MDA-MB-231, and MRC-5 lines were seeded in 24- or 96-well plates at densities of 6 × 10^4 and 1 × 10^4 cells per well, respectively, in culture medium supplemented with 10% fetal bovine serum (FBS). After incubation for 24 h at 37 °C in a humidified atmosphere containing 5% CO_2, the cells were treated with complex B3 at concentrations ranging from 0.51 to 4.04 µM, while control groups received 0.5% DMSO. Morphological changes were monitored at 0, 24, and 48 h using an inverted phase-contrast microscope.

After 48 h of treatment, cells were subjected to fluorescence staining to assess membrane integrity and nuclear morphology. For this, cells were fixed with methanol (50 µL per well, 5 min), followed by staining with CellMask™ Green plasma-membrane stain (1× working solution, 5 min at room temperature) and DAPI (300 nM, 10 min). In parallel, propidium iodide (PI, 300 nM, 200 µL per well) staining was performed for 10 min to identify membrane-compromised cells. After washing twice with PBS, fluorescence images were captured using a CELENA® S

fluorescence microscope (Logos Biosystems, Korea) equipped with filter sets suitable for CellMask Green, DAPI, and PI.

2.3.5. Cell viability assay (LIVE/DEAD®)

A2780cis, MDA-MB-231, and MRC-5 cells were seeded at a density of 10^4 cells/well in 96-well plates containing 150 μL of culture medium supplemented with 10% FBS. The plates were then incubated for 24 h at 37 °C and 5% CO_2. The cells were then treated with different concentrations of the compound PdB3 (1.01 μM, 2.02 μM, 4.04 μM, and 8.08 μM) in addition to a control containing 0.5% DMSO. The cells were then incubated for an additional 48 h.

After this period, 100 μL of LIVE/DEAD® solution, prepared according to the manufacturer's instructions, was added. The cells were incubated for 30 min. The medium was carefully removed and replaced with 100 μL of fresh medium. Images were obtained with a fluorescence microscope (CELENA® S, Logos Biosystems) using a 4× objective.

2.3.6. Wound healing assay

Cells (2×10^5 per well) were seeded in 6-well plates and incubated at 37 °C in a humidified atmosphere with 5% CO_2 for 24 h or until a confluent monolayer (≈100%) was formed. After cell monolayer formation, a scratch was made across the cell surface using a 10 μL pipette tip. The culture medium was then removed, and the wells were gently washed with PBS to eliminate detached cells. Subsequently, fresh medium containing complex B3 at concentrations of 0.51, 1.01, and 2.02 μM was added to each well. Images of the wound area were captured at 0, 24, and 48 h using an inverted microscope (CELENA® S, Logos Biosystems, Korea). The extent of cell migration inhibition was quantified using ImageJ software, and the percentage of wound closure was calculated according to Eq. (1).

$$\%\textit{Wound closure} = \frac{A_{t=0h} - A_{=\Delta h}}{A_{t=0h}}\ x\ 100$$

$$\%\mathrm{Woundclosure} = \frac{\mathrm{A_{t=0h}} - \mathrm{A_{=\Delta h}}}{\mathrm{A_{t=0h}}}\mathrm{xd}\%\mathrm{Woundclosure} = \frac{\mathrm{A_{t=0h}} - \mathrm{A_{=\Delta h}}}{\mathrm{A_{t=0h}}}\mathrm{xd} \quad (1)$$

Where, At = 0 h: measurement of the scratched area at 0 h and At = Δh: measurement of the scratched area at 24 and 48 h. The assay was performed in triplicates.

2.3.7. Cell cycle arrest

Cells from the A2780cis line were seeded in 12-well plates at a density of 2.0×10^5 cells per well and incubated for 24 h at 37 °C in a humidified atmosphere containing 5% CO_2. The cells were then treated with the test compounds at concentrations corresponding to ½ IC_{50}, IC_{50}, and 4 × IC_{50}, in triplicate, and incubated for an additional 48 h under the same conditions. After treatment, the medium was removed, and the cells were washed with PBS, resuspended, and centrifuged at 1000 rpm for 5 min at 4 °C. The supernatant was discarded, and the resulting pellet was fixed with 500 μL of ice-cold 70% ethanol, followed by storage at −20 °C for 24 h. The fixed cells were subsequently washed with PBS, centrifuged again, and resuspended in a solution containing 0.2 mg/mL ribonuclease A (RNase A) and propidium iodide (PI). The suspension was incubated for 30 min at room temperature, protected from light. Flow cytometry was performed using a BD Accuri™ C6 cytometer (BD Biosciences, USA) to determine the percentage of cells in each phase of the cell cycle.

2.3.8. Cell death assay

The induction of cell death by complex B3 was assessed in A2780cis cells by flow cytometry, using an Annexin *V* phycoerythrin (PE)/7-aminoactinomycin D (7-AAD) apoptosis detection kit (BD Biosciences, USA). Cells (1×10^5 per well) were seeded in 12-well plates with 1.5 mL of culture medium and incubated at 37 °C in 5% CO_2 for 24 h. After incubation, the cells were treated with complex B3 at concentrations of 0.25, 1.01, and 4.04 μM, and maintained for an additional 48 h under the same conditions. Following treatment, the culture medium was removed, and the wells were washed with PBS. A 200 μL aliquot of binding buffer (10 mM HEPES/NaOH, 140 mM NaCl, 2.5 mM $CaCl_2$) supplied with the kit was added. The culture medium and PBS fractions were pooled, centrifuged, and the resulting pellet was washed twice with PBS. The cells were resuspended in 70 μL of binding buffer, and 2.5 μL each of Annexin *V*–PE and 7-AAD were added, followed by incubation for 20 min at room temperature, protected from light. Cells were detached using a scraper, centrifuged, and resuspended in 200 μL of binding buffer for analysis. Flow cytometric measurements were carried out using a BD Accuri™ C6 cytometer, and data were analyzed with BD Accuri™ C6 software. Negative controls consisted of cells treated with 0.5% DMSO, positive controls for apoptosis were obtained by camptothecin treatment, and positive controls for necrosis were prepared by heating cells at 80 °C for 2 h, followed by staining with 7-AAD alone. Additional controls included single and double fluorochrome labeling (Annexin *V*–PE and/or 7-AAD) of untreated cells.

2.3.9. 3D morphological cell culture assay

The 3D spheroid assay was conducted using A2780cis cells and the Greiner Bio-One Magnetic Bioprinting Kit (Greiner Bio-One, Austria) for 96-well plates. Cells were first cultured in 25 cm^2 flasks under standard conditions (37 °C, 5% CO_2) until reaching 80% confluence. The cells were washed with 3 mL of PBS, detached with 1 mL of trypsin, neutralized with 2 mL of culture medium, and centrifuged at 1500 rpm for 5 min. The supernatant was discarded, and the pellet was resuspended in 5 mL of fresh medium. Subsequently, 150 μL of magnetic nanoparticles were added to the suspension, which was returned to the culture flask and incubated for 24 h.

After nanoparticle incorporation, the cells were trypsinized and counted using the trypan blue exclusion method. The density was adjusted to 1500 cells per well, and the cells were seeded in repellent 96-well plates placed on a magnetic drive. The plates were incubated for 4 days to allow spheroid formation, with medium replacement every 3 days, following the manufacturer's protocol. After spheroid formation, the cells were treated with complex B3 and cisplatin at concentrations of 1.6, 6.3, 12.5, 50, and 100 μM, along with a control group containing 0.5% DMSO. The evolution of the spheroids was monitored by bright-field microscopy at 0, 48, 96, and 144 h. Spheroid diameters were measured using ImageJ software. All experiments were performed in sextuplicate ($n = 6$).

2.3.10. Statistical analysis

Statistical analyses were performed using GraphPad Prism 8.0.2 software. Results were expressed as mean ± standard deviation (SD). Differences between groups were evaluated by one-way analysis of variance (ANOVA) followed by Dunnett's post hoc test. A p-value <0.05 was considered statistically significant.

3. Results and discussion

3.1. Synthesis and characterization

The Pd(II) complexes were synthesized from cis-$[PdCl_2(CH_3CN)_2]$, prepared according to a literature method [31], by reaction with the respective thiosemicarbazide derivatives (TSC, MetTSC, EtTSC) and diphosphine ligands (dppp or dppb) in a 1:1:1 M ratio, as described in Section 2. The resulting yellow solids were characterized by FTIR, ^{1}H NMR and ^{31}P NMR, high-resolution mass spectrometry (HRMS), and single-crystal X-ray diffraction (SC-XRD). The combined data confirm the successful formation of Pd(II) coordination complexes with the expected stoichiometry and geometry.

In the FTIR spectra, the $\nu(NH_2)$ stretching vibrations of the thiosemicarbazides (3369–3182 cm^{-1}) shifted by >10 cm^{-1} to higher wavenumbers upon complexation, suggesting new hydrogen-bonding

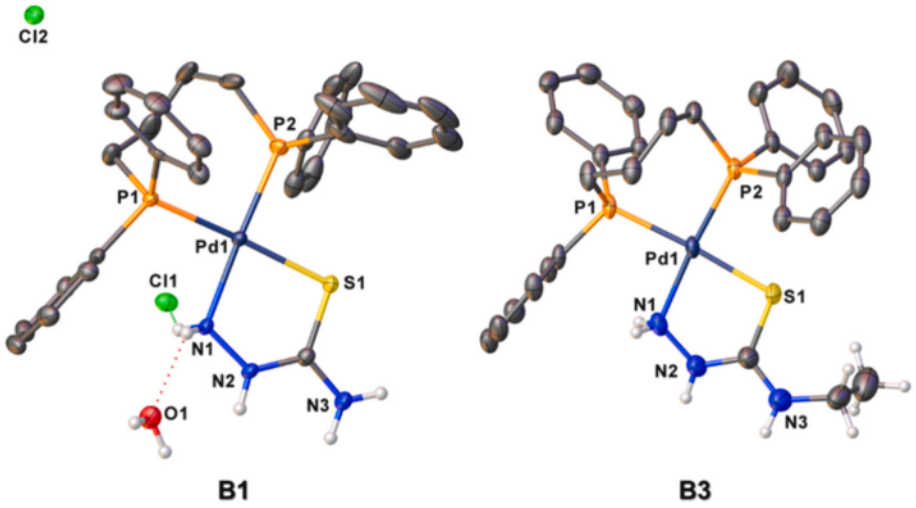

Fig. 1. ORTEP type illustration of the asymmetric unities of B1 and B3, with atomic labelling of the non-C, H atoms. Ellipsoids drawn at 50% of probability. Hydrogen atoms from dppb were omitted for clarity.

interactions. The δ(NH₂) bending modes, initially at 1645 and 1634 cm^{-1}, shifted by 7–15 cm^{-1} to lower energy, and the disappearance of the ν(N–C=S) band (1568–1531 cm^{-1}) indicated coordination through nitrogen (N) and sulfur (S) atoms [32–35]. Characteristic ν(P–Ph) bands from the diphosphine ligands appeared at 1433, 1095, and 696 cm^{-1} [36–38], confirming their involvement in coordination. The FTIR spectra are provided in the Supplementary Material (Fig. S1).

The ^{1}H NMR spectra of the Pd(II) complexes are consistent with the proposed coordination environment and confirm a 1:1 stoichiometric ratio between the thiosemicarbazide and diphosphine ligands. Two main sets of resonances are observed. Signals in the aliphatic region (δ 1.0–3.5 ppm) are assigned to protons of the diphosphine backbones and alkyl substituents of the thiosemicarbazide derivatives, whereas resonances between δ 7.0 and 8.0 ppm correspond to the aromatic protons of the diphenylphosphine groups. For complexes P2 and B2, a singlet at δ 2.81 ppm is attributed to the methyl group (–CH₃) of the 4-MeTSC ligand. In complexes P3 and B3, a triplet at δ 1.04 ppm is assigned to the terminal methyl group of the ethyl substituent of 4-EtTSC, while a multiplet at δ 3.11–2.99 ppm, integrating for four protons, is attributed to overlapping methylene (–CH₂–) resonances from the diphosphine ligand and the ethyl fragment of 4-EtTSC.

The NH proton of the thiosemicarbazide moiety is observed at δ 7.92 ppm in complexes P1, P3, B1, and B2; however, in some cases, the most deshielded NH signal is not detected. This behavior is attributed to coordination-induced NH lability, resulting in fast proton exchange with the deuterated solvent (MeOD) and signal broadening beyond detection. The NH₂ resonances are likewise not clearly resolved, consistent with rapid exchange and/or partial deprotonation processes in solution. Such features are commonly reported for metal–thiosemicarbazide complexes and are compatible with N,S-bidentate coordination. Additionally, the terminal CH₃ resonance of the ethyl-substituted thiosemicarbazide in complex P3 is significantly broader than in B3, which is possibly attributed to local dynamic effects of the ethyl group within the more rigid DPPP chelate, including restricted rotation and slow conformational fluctuations leading to exchange broadening on the ^{1}H NMR timescale.

In the $^{31}P\{^{1}H\}$ NMR, the free ligands dppp and dppb showed singlets at −17.7 and − 13.5 ppm, respectively. Upon complexation, these signals shifted to the positive region and split into two doublets, revealing magnetically non-equivalent phosphorus atoms. The more deshielded doublet corresponds to P *trans* to S, while the other is assigned to P *trans* to N. The measured ^{2}J(P-P) coupling constants support a bidentate coordination mode of the diphosphine ligands to Pd(II) [39–41]. Full ^{1}H and $^{31}P\{^{1}H\}$ NMR spectra are available in the Supplementary Material (Figs. S2–S13).

High-resolution mass spectrometry (HRMS) further corroborated the proposed formulations. All complexes exhibited the expected $[M - H]^{+}$ molecular ion and the characteristic palladium isotopic pattern (1:1). Additionally, isotopic envelopes corresponding to $[M]^{2+}$ species ($m/z \approx$ 1:2) were observed for complexes P2, P3, B2, and B3, confirming the presence of doubly charged Pd(II) ions. The HRMS spectra are included in the Supplementary Material (Figs. S14–S29).

Crystals of complexes B1 and B3 suitable for X-ray diffraction were obtained by slow evaporation of a chloroform/methanol (2:1, *v*/v) solution at 25 °C. Single-crystal X-ray diffraction analysis revealed that the dppb ligand coordinates in a bidentate manner to the metal center,

Table 1
Cytotoxicity (IC_{50}) and selectivity index (SI).

Compounds	MRC-5	A549	DU-145	A2780	A2780cis	MCF-7	MDA-MB-231	*SI	**SI
P1	>50	>50	>50	>50	>50	>50	>50	–	–
P2	>50	>50	>50	16.40 ± 0.30	16.04 ± 0.64	32.17 ± 1.60	31.25 ± 0.67	>3.12	>1.6
P3	14.45 ± 0.22	>50	>50	3.76 ± 0.06	1.70 ± 0.11	19.28 ± 0.37	3.28 ± 0.28	8.50	4.41
B1	>50	>50	>50	7.34 ± 0.36	21.5 ± 0.37	29.05 ± 0.55	37.04 ± 0.27	>2.32	>1.35
B2	14.43 ± 0.17	>50	>50	4.45 ± 0.5	9.44 ± 0.16	21.22 ± 0.71	8.67 ± 0.27	1.53	1.67
B3	15.54 ± 1.21	>50	>50	1.09 ± 0.07	0.99 ± 0.15	12.26 ± 0.98	1.01 ± 0.08	15.69	15.38
Cisplatin	12.47 ± 0.15	14.40 ± 1.40	2.3 ± 0.4	11.17 ± 0.30	25.61 ± 0.29	13.9 ± 2.0	>50	0.50	0.25<
dppp	>50	>50	>50	>50	>50	>50	>50	–	–
dppb	>50	>50	>50	>50	>50	>50	>50	–	–
TSC	>50	>50	>50	>50	>50	>50	>50	–	–
MeTSC	>50	>50	>50	>50	>50	>50	>50	–	–
EtTSC	>50	>50	>50	>50	>50	>50	>50	–	–

*SI: (MRC5/A2780 Cis) **SI: (MRC5/MDA-MB-231).

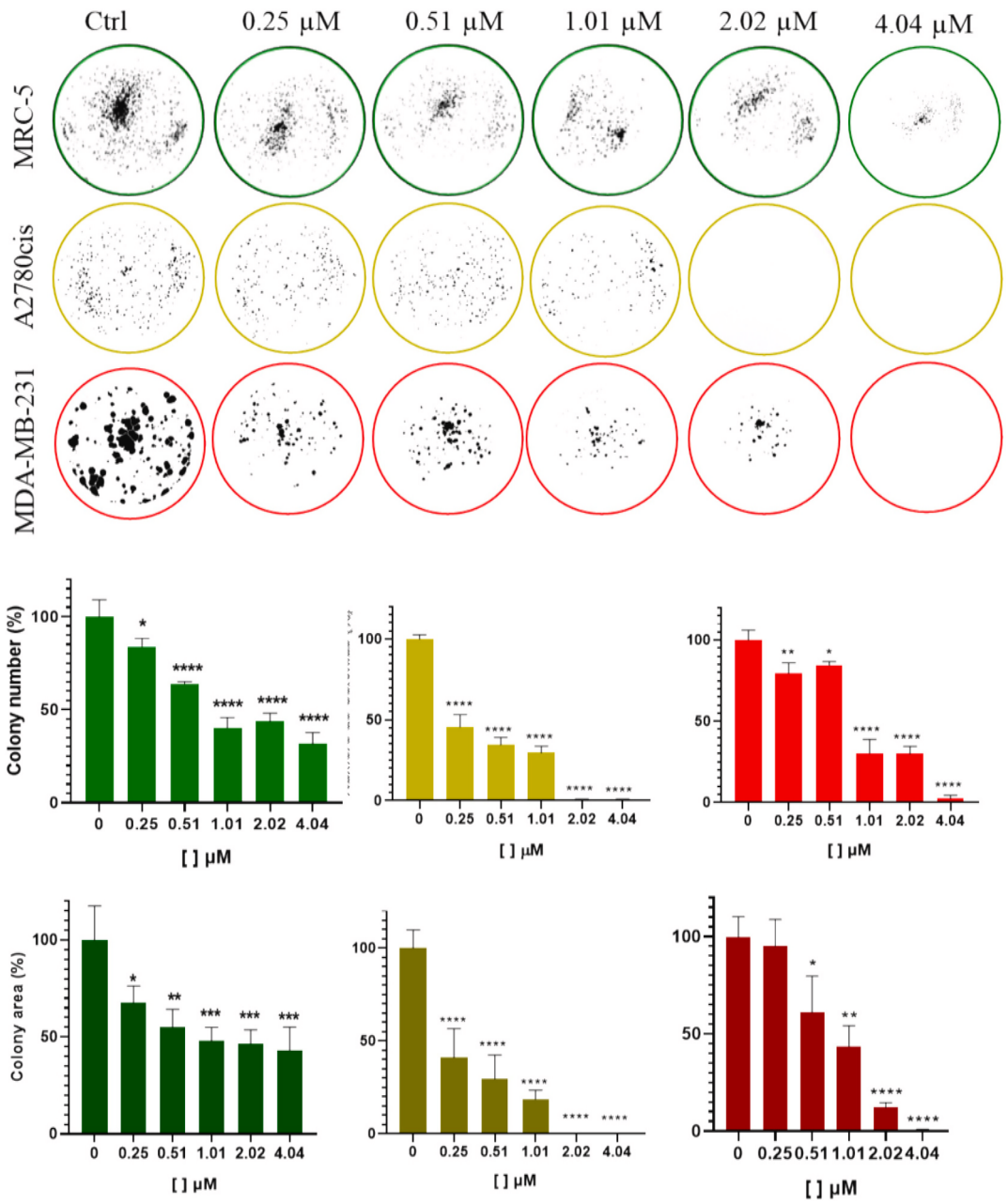

Fig. 2. Images of MRC-5, A2780cis and MDA-MB-231 colonies treated with different concentrations of the B3 compound and the distribution of the number and area of colonies (%) (green - MRC-5), (yellow - A2780cis) and (red - MDA-MB-231). Significance values: $*p = 0.01$ $**p = 0.004$ $***p = 0.0003$ and $****p < 0.0001$. (For interpretation of the references to colour in this figure legend, the reader is referred to the web version of this article.)

forming a seven-membered chelate ring. The N1 and S1 atoms of the thiosemicarbazide ligands also coordinate bidentately in a *cis* arrangement, generating a five-membered ring. The resulting complexes exhibit a distorted square-planar geometry around the Pd(II) center in their dicationic (2^+) form, with chloride ions acting as counter-ions (Fig. 1). Crystallographic parameters and refinement details are summarized in Table S1 of the Supplementary Material.

3.1.1. Cell viability

We evaluated the antiproliferative activity of palladium(II) complexes in a panel of human cancer and non-tumor cell lines using the MTT assay. Then, we compared the IC_{50} values with those of cisplatin after 48 h of incubation (Table 1). For easier interpretation, the complexes were divided into two groups based on the diphosphine ligand: group P contains 1,3-bis(diphenylphosphino)propane (dppp), and group B contains 1,4-bis(diphenylphosphino)butane (dppb). Within each series, systematic modifications to the thiosemicarbazide moiety enabled evaluation of the effects of substituents on biological activity.

In both series, a trend was observed in which the substitution of the thiosemicarbazide ligand followed the order TSC < MeTSC < EtTSC. This correlates with a systematic increase in antiproliferative potency. This pattern reveals a positive structure–activity relationship associated with the incremental growth of the alkyl substituent ($–CH_3$, $–C_2H_5$). Similar effects of alkyl substitution on cytotoxicity have been reported for related Pd(II) and Ru(II) complexes containing thiosemicarbazone or thiosemicarbazide derivatives [42–44].

A comparison of the two ligand systems revealed that dppb-based complexes (group B) generally exhibited higher cytotoxicity than their dppp analogues (group P). The longer four-carbon chain of the dppb ligand provides higher flexibility to the chelate ring and modifies the

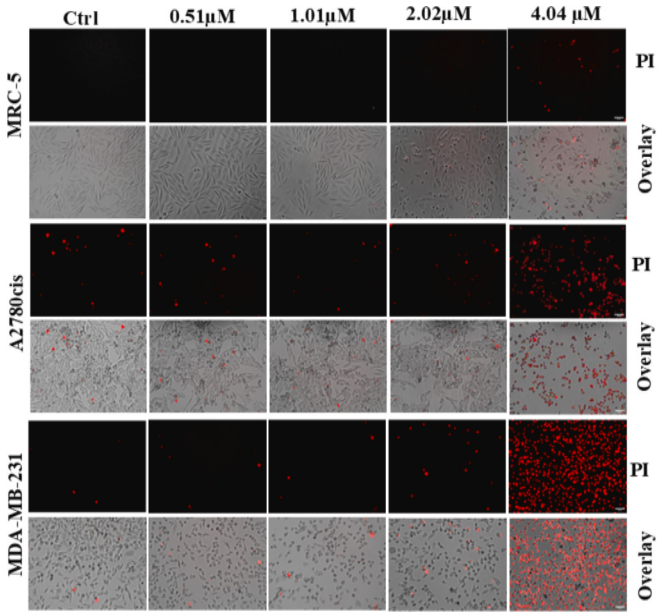

Fig. 3. Cellular morphology of MRC-5, A2780cis and MDA-MDB-231 cells treated with compound B3 and cells stained with PI. Images obtained with special CELENA® S with 10× objective. Scale bars = 50 μm.

steric and electronic environment around the metal center. These features can influence the strength of the metal–ligand bond and the accessibility of Pd(II) to biomolecular sites, such as nucleic acids and sulfur-rich proteins [16,39–41]. Thus, the phosphine ligand plays a key role in modulating biological activity, functioning not only as a structural scaffold, but also as an electronic and steric regulator of the metal's bioactivity.

Complex B3 [Pd(dppb)(4-EtTSC)]Cl_2 was identified as the most potent compound, with IC_{50} values of approximately 1.0 μM against breast (MDA-MB-231) and ovarian (A2780 and A2780cis) cancer cell lines. Remarkably, B3 demonstrated 25–30-fold higher cytotoxicity and selectivity than cisplatin, with selectivity index (SI) values of approximately 15 toward tumor versus non-tumor (MRC-5) fibroblast cells. Its strong activity against the cisplatin-resistant A2780cis line highlights its potential to overcome platinum resistance mechanisms. This may be due to distinct uptake routes or different modes of interaction with intracellular targets.

These findings suggest a structure-activity relationship, where variations in the phosphine and thiosemicarbazide ligands influence the response of the complexes. These observations contribute to understanding the structural factors that affect the biological behavior of Pd (II)-based compounds.

3.1.2. *Clonogenic assay*

The clonogenic assay was performed to investigate the long-term cytotoxic and cytostatic effects of the Pd(II) complexes, as this method assesses the ability of individual cells to survive, proliferate, and form colonies after drug exposure [42], [43]. Among the tested compounds, complex B3 was selected for further analyses due to its pronounced antiproliferative activity in 2D assays.

As shown in Fig. 2, B3 exhibited a dose-dependent reduction in both colony number and area for the A2780cis and MDA-MB-231 tumor cell lines. Increasing concentrations of the compound progressively suppressed clonogenic capacity, leading to nearly complete inhibition of colony formation at 2.02 μM for A2780cis and 4.04 μM for MDA-MB-231 cells. The observed decrease in colony size suggests not only reduced survival but also potential interference with the proliferative potential of surviving cells. These effects are consistent with cytostatic and/or cytotoxic mechanisms that compromise the long-term reproductive viability of tumor populations.

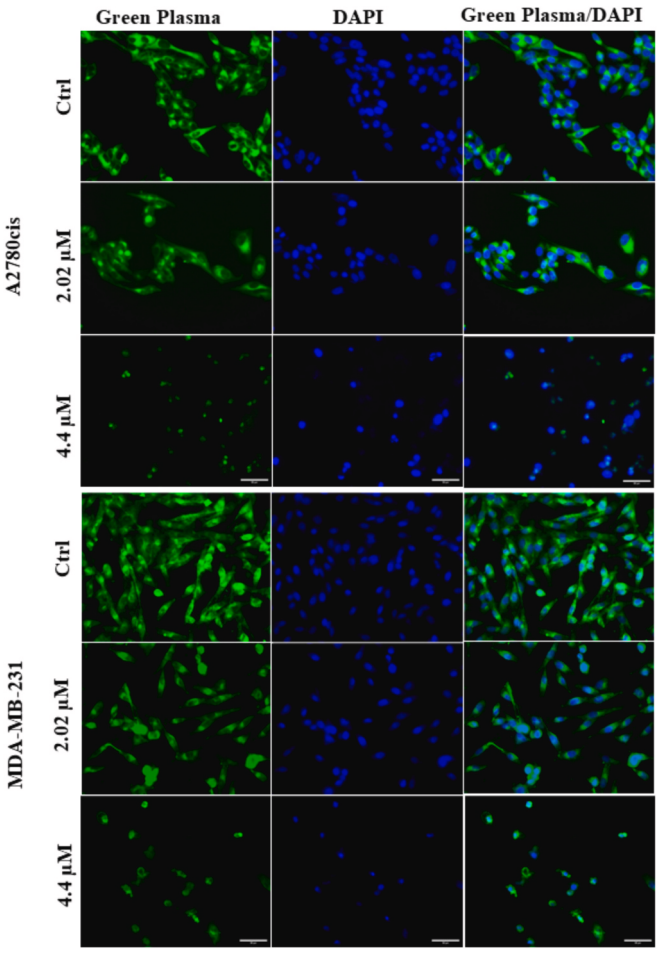

Fig. 4. Fluorescence morphological assay of A2780cis and MDA-MB-231 cells treated with B3 and stained with Green Plasma (green) and DAPI (blue). Images obtained with a CELENA® S microscope with 20× objective. Scale bars = 50 μm. (For interpretation of the references to colour in this figure legend, the reader is referred to the web version of this article.)

In contrast, the non-tumor MRC-5 fibroblast cells maintained a higher clonogenic capacity under equivalent treatment conditions, indicating greater resistance to B3 exposure. This observation agrees with the selectivity pattern obtained in the MTT assays, suggesting that B3 exerts a preferential antiproliferative effect toward malignant cells. Although the underlying mechanism remains to be clarified, such differential responses may reflect differences in membrane composition or DNA repair capacity between tumor and normal cells.

3.1.3. *Cell morphology*

A morphological analysis was performed to qualitatively evaluate the cellular responses induced by complex B3 in tumor (A2780cis and MDA-MB-231) and non-tumor (MRC-5) cell lines 48 h after treatment. This approach complements viability and clonogenic data by revealing visible alterations in cell structure and integrity.

As illustrated in Fig. 3, both tumor cell lines exhibited progressive morphological changes with increasing B3 concentrations. At low concentrations, the cells exhibited slight reductions in confluence and slight shape irregularities, indicating early cytostatic effects. At concentrations around 2× IC_{50} (2.02 μM), there was a significant decrease in cell density accompanied by cell rounding and partial detachment from the substrate. At the highest tested concentration (4× IC_{50}, 4.04 μM), cells exhibited pronounced size reduction, membrane blebbing, and debris accumulation, which are typical features of apoptosis or late-stage cell

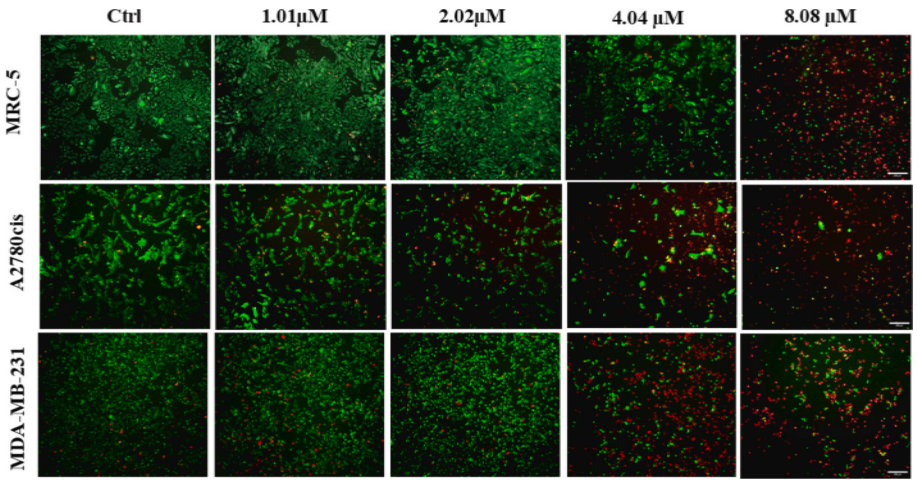

Fig. 5. Micrographs of MRC-5, A2780cis and MDA-MB-231 cells treated with the B3 compound and labeled with the Kit: LIVE/DEAD after 48 h of treatment (green cells = viable cells and red cells = dead cells). Images obtained with a CELENA® S microscope with 4× objective. Scale bars = 200 µm. (For interpretation of the references to colour in this figure legend, the reader is referred to the web version of this article.)

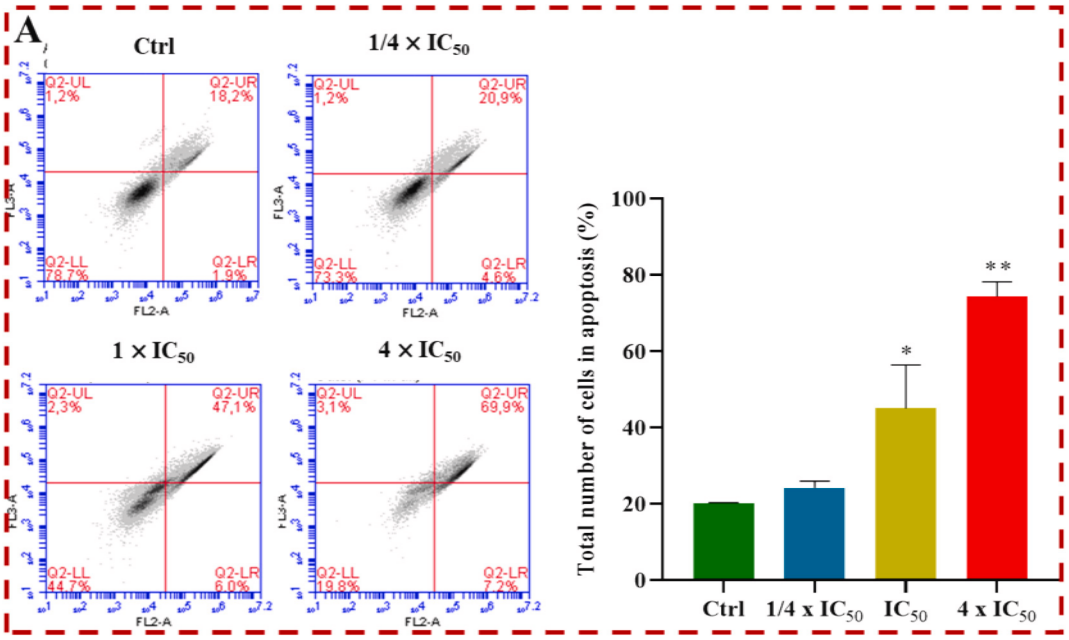

Fig. 6. Histogram of the distribution of cell death treated with different concentrations of the compound B3, Q1 - necrosis, Q2 - viable cells, Q3 - early apoptosis and Q4 - late apoptosis and graph of the percentage of total cell death (early apoptosis + late apoptosis). Significance level $*p = 0.03$ and $**p = 0.002$.

death [45–49].

Fluorescent staining with propidium iodide (PI) confirmed loss of membrane integrity at higher concentrations, while CellMask Green/DAPI labeling revealed chromatin condensation and nuclear fragmentation (Fig. 4) [50–52]. These changes were considerably less evident in MRC-5 fibroblasts, indicating greater tolerance of non-tumor cells to B3 exposure.

While these preliminary findings align with the cytotoxic trends observed in other assays, they should be interpreted cautiously. The morphological alterations suggest possible involvement of apoptosis, but additional mechanistic studies, such as flow cytometry-based apoptosis quantification and mitochondrial potential assays, are needed to confirm the pathways responsible for the observed effects.

3.1.4. Live/dead assay

The Live/Dead fluorescence assay was used to visualize and qualitatively evaluate cell viability after exposure to complex B3. This method complements morphological and clonogenic analyses by directly distinguishing between viable (green) and non-viable (red) cells and providing an overview of the compound's cytotoxic profile [53,54].

As illustrated in Fig. 5, treatment with B3 resulted in a gradual decrease in the percentage of viable cells in both the A2780cis and the MDA-MB-231 tumor lines. This is consistent with the dose-dependent loss of viability observed in the MTT and colony formation assays. At higher concentrations (≥2.02 µM), fluorescence images revealed a significant increase in red-stained cells, indicating extensive membrane disruption and decreased metabolic activity. In contrast, the non-tumor MRC-5 fibroblasts maintained predominantly green fluorescence even at the highest tested concentrations, suggesting these cells are less sensitive to B3 exposure. These qualitative data reinforce the selective cytotoxic trend of complex B3 toward tumor cells and support its potential as a targeted antiproliferative agent.

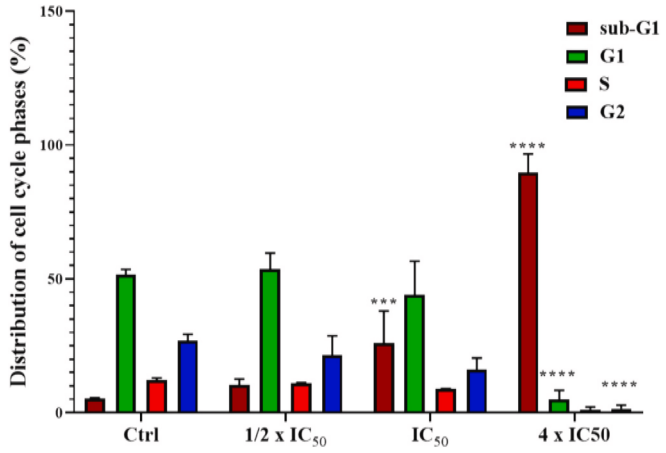

Fig. 7. Distribution graph of cell counts for cell cycle phases (sub-G1, G1, S and G2) treated with B3 compound. Significance level ***$p = 0.0002$ and ****$p < 0.0001$.

3.1.5. Cell death assay

In multicellular organisms, cell death can occur through distinct biochemical and morphological pathways. The most described processes are apoptosis and necrosis [55,56]. To investigate the type of cell death induced by complex B3, flow cytometry analyses were performed using the Annexin V-PE/7-AAD assay on the A2780cis ovarian tumor cell line.

As shown in Fig. 6, treatment with B3 resulted in a dose-dependent increase in apoptotic cell populations, while the percentage of necrotic cells remained low across all tested concentrations. After 48 h, approximately 50% of cells underwent apoptosis at the IC_{50} concentration (1.01 μM), rising to approximately 77% at the 4× IC_{50} concentration (4.04 μM). This profile indicates that B3 primarily promotes programmed cell death rather than non-specific necrosis, consistent with its controlled and selective cytotoxic behavior.

These findings align with morphological and cell cycle analyses revealing apoptotic features, such as chromatin condensation, cell size reduction, and DNA fragmentation. While the data suggest a predominance of apoptotic mechanisms, these are preliminary results. From a pharmacological standpoint, preferential induction of apoptosis is desirable because it minimizes the inflammatory responses typically associated with necrosis and may contribute to better therapeutic selectivity [60–62].

3.1.6. Cell cycle arrest

The effect of complex B3 on the cell cycle distribution of the A2780cis ovarian tumor cell line was evaluated by flow cytometry after 48 h of treatment at concentrations corresponding to 1/2 IC_{50}, IC_{50}, and 4× IC_{50}. The goal of this analysis was to identify potential alterations in cell cycle progression that could contribute to the compound's antiproliferative effects.

As shown in Fig. 7, higher concentrations of B3 resulted in an accumulation of cells in the sub-G1 phase and a reduction in the G1 and S phase populations. At the IC_{50} concentration (1.01 μM), approximately 26% of cells were in the sub-G1 phase. At the 4 × IC_{50} concentration (4.04 μM), this fraction increased to nearly 90%. The sub-G1 population is associated with DNA fragmentation, a hallmark of apoptosis [57–59]. These results align with morphological and apoptosis assays, indicating that B3 induces cell cycle disruption and programmed cell death in a concentration-dependent manner.

3.1.7. Wound healing

A wound healing assay was performed to investigate the effect of complex B3 on tumor cell migration [50], [51]. As shown in Fig. 8, B3 treatment resulted in a clear, concentration-dependent reduction in wound closure in both the A2780cis and the MDA-MB-231 cell lines. Notably, statistically significant inhibition of wound closure was observed at the lowest tested concentration (0.51 μM), particularly in

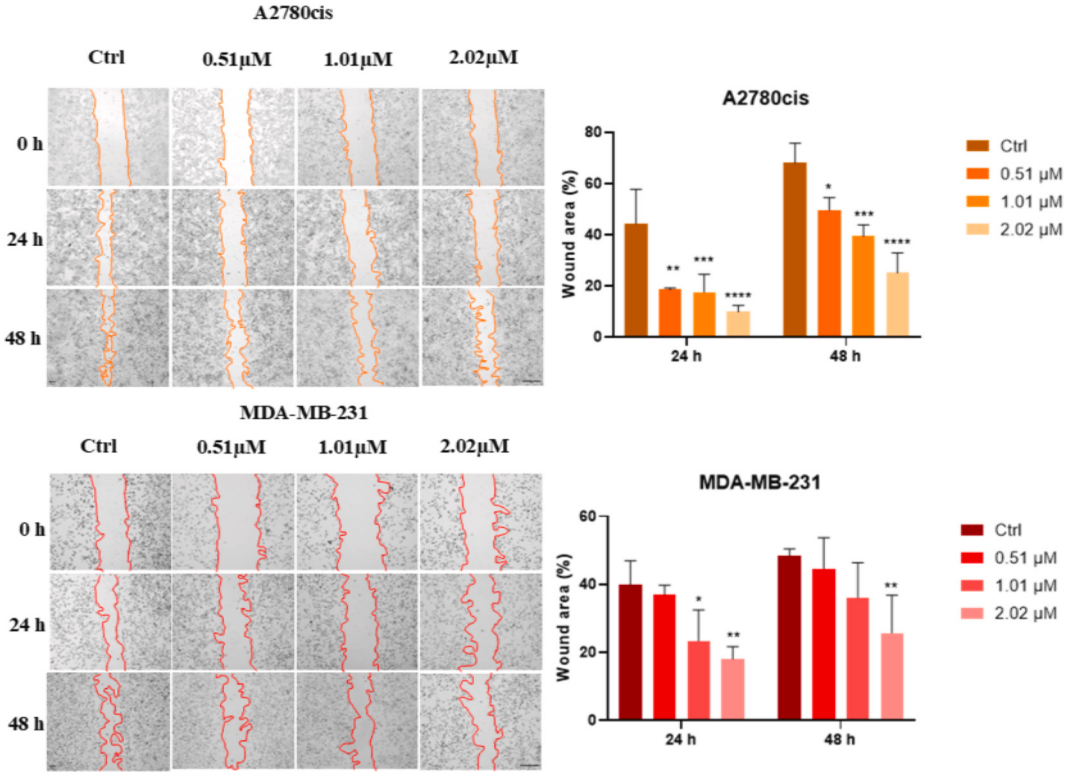

Fig. 8. Wound closure assay of the B3 compound in A2780cis and MDA-MB-231 cell lines. Significance values: *$p = 0.02$, **$p = 0.06$ and *$p = 0.0001$. Images obtained with a CELENA® S microscope with 10× objective. Scale bars = 100 μm.

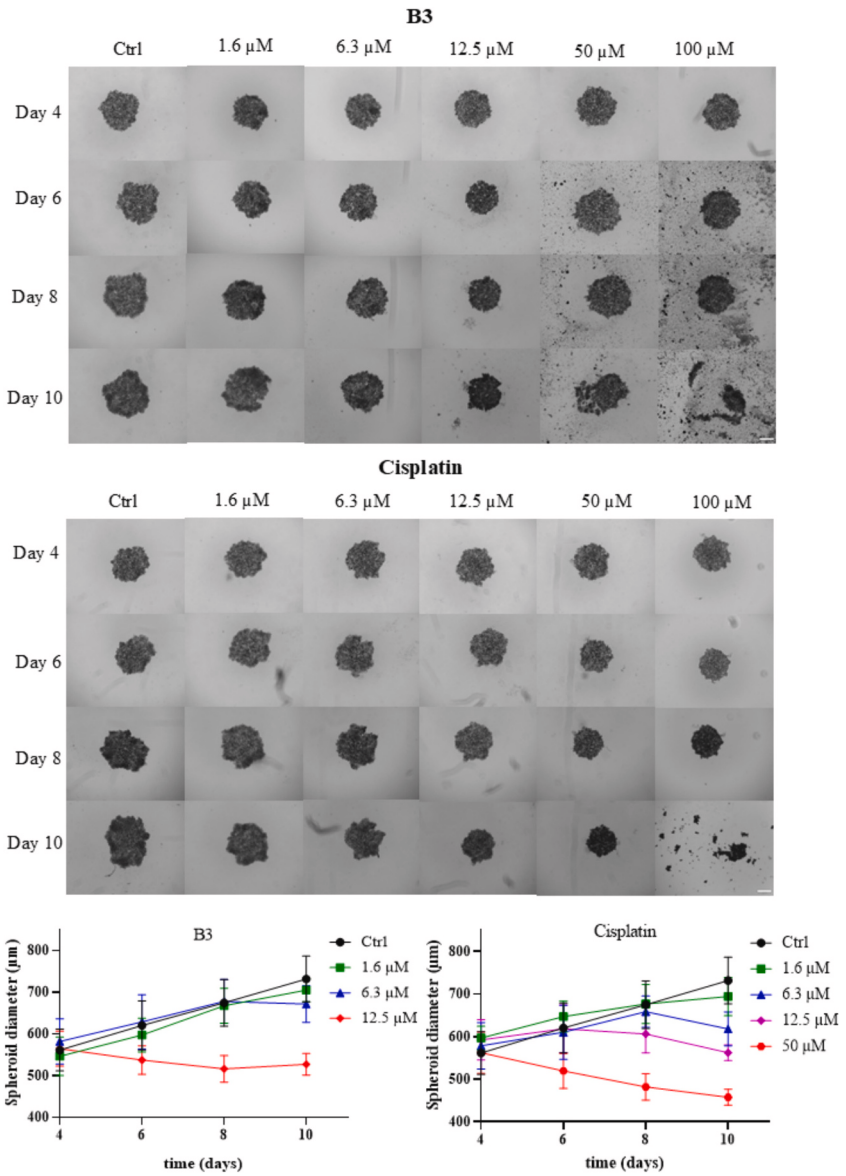

Fig. 9. Morphology of A2780cis cell spheroids treated with B3 and cisplatin. Diameter of spheroids treated B3 and cisplatin. Images obtained with a CELENA® S microscope with 4× objective. Scale bars = 200 µm.

A2780cis cells. Stronger effects were observed at 1.01 and 2.02 µM. The response was more pronounced overall in the cisplatin-resistant ovarian cancer model.

At the tested concentrations (0.51–2.02 µM), B3 did not induce acute cytotoxicity within 48 h, as determined by morphological inspection and Live/Dead staining. However, the concentrations of 1.01 and 2.02 µM approach the upper range of biologically active doses. These concentrations are sufficient to impose marked cytostatic stress, which may limit cell proliferation during the assay timeframe. Consequently, the reduced wound closure is primarily attributed to growth inhibition, though impaired cell motility may have contributed as well. This distinction reflects an inherent limitation of wound healing assays performed at concentrations near cytotoxic thresholds, a limitation that was taken into account when interpreting the results.

Overall, these data indicate that B3 exerts a measurable biological effect on wound closure, even at submicromolar concentrations. This finding supports the pronounced cellular activity of B3 and underscores the need for complementary migration-specific assays to fully disentangle the antiproliferative and antimigratory contributions.

3.1.8. Morphological analysis in 3D cell culture

The 3D spheroid model was used to study the behavior of tumor cells in more physiologically relevant conditions. Morphological analysis was performed on complex B3, which exhibited the most effective antiproliferative activity in vitro, as well as on cisplatin, which was used as a reference drug in the A2780cis cell line (Fig. 9). The spheroids reached a suitable size and level of compactness by the fourth day of incubation. Treatment with the compounds was initiated at this point.

Fig. 9 shows that spheroids treated with B3 at concentrations of 1.6–6.3 µM continued to grow steadily up to day 10. However, at 12.5 µM, a visible reduction in spheroid diameter occurred after 48 h. At higher concentrations (50 and 100 µM), progressive structural disintegration and fragmentation occurred, suggesting a loss of spheroid integrity. Cisplatin produced similar effects, but only at higher concentrations. Significant reduction in size began at 50 µM, and fragmentation was evident at 100 µM. These preliminary observations suggest that B3 may exert its effects at lower concentrations than cisplatin under 3D conditions.

On day 10, the spheroids were stained with DAPI/PI to assess cell viability. As shown in Fig. 10, PI fluorescence, which indicates

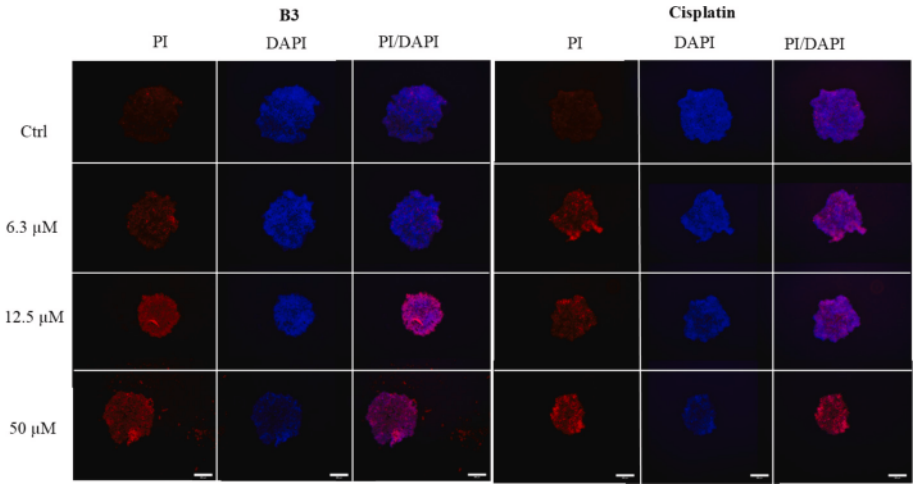

Fig. 10. Images of spheroids with fluorescent markers PI and DAPI treated with B3 and cisplatin after 10 days. Images obtained with a CELENA® S microscope with 4× objective. Scale bars = 200 µm.

membrane compromise, became more intense and widespread at 12.5 µM for B3 and at 50 µM for cisplatin. These findings suggest that the reductions in spheroid size and structural cohesion observed are associated with cell death processes.

Although cellular alterations occurred at higher concentrations in the 3D system than in 2D assays, this difference is expected, given the increased complexity and diffusion barriers inherent to spheroid models. Overall, these preliminary data indicate that B3 maintains significant activity under 3D culture conditions and warrant further investigation using quantitative viability assays and molecular analyses to confirm its performance and mechanism of action.

4. Conclusions

This work presents the synthesis and comprehensive characterization of six novel Pd(II) complexes containing thiosemicarbazide derivatives and diphosphine ligands (dppp or dppb). Spectroscopic and crystallographic analyses confirmed the N,S-bidentate coordination mode of the thiosemicarbazides and the chelating behavior of the diphosphine ligands. This resulted in stable square-planar geometries. Among this series of compounds, [Pd(dppb)(4-EtTSC)]Cl_2 (B3) exhibited exceptional cytotoxic activity, with IC_{50} values approaching 1 µM in breast and ovarian cancer cell lines. Furthermore, it demonstrated low toxicity toward non-tumor fibroblasts. Mechanistic studies indicate that B3 suppresses colony formation and cell migration, induces cell-cycle arrest, and triggers apoptosis in a dose-dependent manner without promoting necrosis. Notably, B3 retained its antiproliferative efficacy against cisplatin-resistant ovarian cells and in 3D tumor spheroid cultures, highlighting its therapeutic potential under physiologically relevant conditions. The combination of enhanced selectivity, potency, and activity against resistant phenotypes highlights the promise of this class of Pd(II) complexes as prototypes for developing new palladium-based metallodrugs.

CRediT authorship contribution statement

Dario B. Fortaleza: Writing – original draft, Methodology, Investigation, Formal analysis, Conceptualization. **Josias S. Rocha:** Writing – review & editing, Investigation, Formal analysis. **George B.S. Pereira:** Methodology, Investigation, Formal analysis. **Tamara Teixeira:** Writing – original draft, Methodology, Investigation, Formal analysis, Data curation. **Jocely L. Dutra:** Methodology, Formal analysis. **Carlos A.F. Moraes:** Formal analysis, Data curation. **Pedro H.O. Santiago:** Methodology, Investigation, Formal analysis. **Alzir A. Batista:** Writing – review & editing, Supervision, Resources. **Moacir R. Forim:** Writing – review & editing, Software, Resources, Data curation. **Javier A. Ellena:** Software, Resources, Data curation. **Fillipe V. Rocha:** Writing – review & editing, Validation, Supervision, Resources, Project administration, Funding acquisition, Data curation, Conceptualization.

Declaration of competing interest

There are no conflicts to declare.

Acknowledgements

F.V.R. thanks the São Paulo Research Foundation (FAPESP, process 2022/02876-0; 2014/50918-7), Funding for Studies and Projects (FINEP) through Grant Agreement No. 01.22.0182, National Council for Scientific and Technological Development (305259/2025-3; 465357/2014-8 CNPq) and CAPES (Finance Code 001). P.H.O.S. and J.E. thank the FAPESP (processes 2017/15850-0 and 2021/10066-5).

Appendix A. Supplementary data

Supplementary data to this article can be found online at https://doi.org/10.1016/j.jinorgbio.2026.113234.

References

[1] M.R. Stratton, P.J. Campbell, P.A. Futreal, The cancer genome, Nature 458 (7239) (2009) 719–724.
[2] B.A.J. Ponder, Cancer genetics, Nature 411 (6835) (2001) 336–341.
[3] D. Hanahan, R.A. Weinberg, Hallmarks of cancer: the next generation, Cell 144 (5) (2011) 646–674.
[4] G. Bergers, S.-M. Fendt, The metabolism of cancer cells during metastasis, Nat. Rev. Cancer 21 (3) (2021) 162–180.
[5] M. Bacac, I. Stamenkovic, Metastatic cancer cell, Annu. Rev. Pathol. Mech. Dis. 3 (2008) 221–247.
[6] F. Bray, et al., Global cancer statistics 2022: GLOBOCAN estimates of incidence and mortality worldwide for 36 cancers in 185 countries, CA Cancer J. Clin. 74 (3) (2024) 229–263.
[7] C. Zhang, C. Xu, X. Gao, Q. Yao, Platinum-based drugs for cancer therapy and anti-tumor strategies, Theranostics 12 (5) (2022) 2115.
[8] S. Rottenberg, C. Disler, P. Perego, The rediscovery of platinum-based cancer therapy, Nat. Rev. Cancer 21 (1) (2021) 37–50.
[9] S. Dilruba, G.V. Kalayda, Platinum-based drugs: past, present and future, Cancer Chemother. Pharmacol. 77 (2016) 1103–1124.
[10] S. Ghosh, Cisplatin: the first metal based anticancer drug, Bioorg. Chem. 88 (2019) 102925.
[11] T.C. Johnstone, K. Suntharalingam, S.J. Lippard, The next generation of platinum drugs: targeted Pt (II) agents, nanoparticle delivery, and Pt (IV) prodrugs, Chem. Rev. 116 (5) (2016) 3436–3486.

[12] M. Ashiq, M. Danish, M.A. Mohsin, S. Bari, F. Mukhtar, Chemistry of platinum and palladium metal complexes in homogeneous and heterogeneous catalysis: a mini review, Int. J. Sci. Basic Appl. Res 7 (1) (2013) 50–61.
[13] R. Czarnomysy, D. Radomska, O.K. Szewczyk, P. Roszczenko, K. Bielawski, Platinum and palladium complexes as promising sources for antitumor treatments, Int. J. Mol. Sci. 22 (15) (2021) 8271.
[14] A.S. Abu-Surrah, H.H. Al-Sa'doni, M.Y. Abdalla, Palladium-based chemotherapeutic agents: Routes toward complexes with good antitumor activity, Cancer Ther. 6 (1) (2008) 1–10.
[15] E.Z. Jahromi, A. Divsalar, A.A. Saboury, S. Khaleghizadeh, H. Mansouri-Torshizi, I. Kostova, Palladium complexes: new candidates for anti-cancer drugs, J. Iran. Chem. Soc. 13 (2016) 967–989.
[16] A.R. Kapdi, I.J.S. Fairlamb, Anti-cancer palladium complexes: a focus on PdX 2 L 2, palladacycles and related complexes, Chem. Soc. Rev. 43 (13) (2014) 4751–4777.
[17] A. Kumar, R. Mishra, A. Mazumder, R. Mazumder, S. Varshney, Exploring synthesis and chemotherapeutic potential of thiosemicarbazide analogs, Anti-cancer Agents Med. Chem. (Form. Curr. Med. Chemistry-anti-cancer Agents) 23 (1) (2023) 60–75.
[18] P.T. Acharya, Z.A. Bhavsar, D.J. Jethava, D.B. Patel, H.D. Patel, A review on development of bio-active thiosemicarbazide derivatives: recent advances, J. Mol. Struct. 1226 (2021) 129268.
[19] V. Pantea, V. Cobzac, O. Tagadiuc, V. Palarie, V. Gudumac, In vitro evaluation of the cytotoxic potential of thiosemicarbazide coordinating compounds in hepatocyte cell culture, Biomedicines 11 (2) (2023) 366.
[20] P. Kozyra, et al., Potential anticancer agents against melanoma cells based on an as-synthesized thiosemicarbazide derivative, Biomolecules 12 (2) (2022) 151.
[21] N. Mirzadeh, T.S. Reddy, S.K. Bhargava, Advances in diphosphine ligand-containing gold complexes as anticancer agents, Coord. Chem. Rev. 388 (2019) 343–359.
[22] C.K. Mirabelli, et al., Antitumor activity of bis (diphenylphosphino) alkanes, their gold (I) coordination complexes, and related compounds, J. Med. Chem. 30 (12) (1987) 2181–2190.
[23] R.M. Snyder, et al., Modulation of the antitumor and biochemical properties of bis (diphenylphosphine) ethane with metals, Cancer Res. 46 (10) (1986) 5054–5060.
[24] S. Breslin, L. O'Driscoll, Three-dimensional cell culture: the missing link in drug discovery, Drug Discov. Today 18 (5–6) (2013) 240–249.
[25] A.G. Souza, I.C.C. Ferreira, K. Marangoni, V.A.F. Bastos, V.A. Goulart, Advances in cell culture: more than a century after cultivating cells, J. Biotechnol. Biomater. 6 (2016) 2–5.
[26] K.M. Yamada, E. Cukierman, Modeling tissue morphogenesis and cancer in 3D, Cell 130 (4) (2007) 601–610.
[27] F. Foglietta, L. Serpe, R. Canaparo, The effective combination between 3D cancer models and stimuli-responsive nanoscale drug delivery systems, Cells 10 (12) (2021) 3295.
[28] K. Brajša, M. Trzun, I. Zlatar, D. Jelić, Three-dimensional cell cultures as a new tool in drug discovery, Period. Biol. 118 (1) (2016) 59–65.
[29] G.M. Sheldrick, Crystal structure solution with ShelXT, Acta Crystallogr. A 71 (2015) 3–8.
[30] O.V. Dolomanov, L.J. Bourhis, R.J. Gildea, J.A.K. Howard, H. Puschmann, OLEX2: a complete structure solution, refinement and analysis program, J. Appl. Crystallogr. 42 (2) (2009) 339–341, https://doi.org/10.1107/S0021889808042726.
[31] S. Komiya, Synthesis of Organometallic Compounds: A Practical Guide 15, John Wiley & Sons, 1997.
[32] P. Patel, B.V. Agarwala, Synthesis and IR spectral study of semicarbazone and thiosemicarbazones of 4-methyl-2-pentanone and their metal complexes, Synth. React. Inorgan. Metal-Organ. Chem. 26 (10) (1996) 1637–1650.
[33] J. Devi, M. Yadav, D.K. Jindal, D. Kumar, Y. Poornachandra, Synthesis, spectroscopic characterization, biological screening and in vitro cytotoxic studies of 4-methyl-3-thiosemicarbazone derived Schiff bases and their Co (II), Ni (II), Cu (II) and Zn (II) complexes, Appl. Organomet. Chem. 33 (10) (2019) e5154.
[34] N.M. El-Metwally, G.A.A. Al-Hazmi, Spectroscopic evaluation for VO (II), Ni (II), Pd (II) and Cu (II) complexes derived from thiosemicarbazide: a special emphasis on EPR study and DNA cleavage, Spectrochim. Acta A Mol. Biomol. Spectrosc. 107 (2013) 289–295.
[35] B.Ş. Yüksel, Spectroscopic characterization (IR and NMR), structural investigation, DFT study, and Hirshfeld surface analysis of two zinc (II) 2-acetylthiophenyl-thiosemicarbazone complexes, J. Mol. Struct. 1229 (2021) 129617.
[36] A. Shanmugapriya, R. Jain, D. Sabarinathan, G. Kalaiarasi, F. Dallemer, R. Prabhakaran, Structurally different mono-, bi-and trinuclear Pd (II) complexes and their DNA/protein interaction, DNA cleavage, and anti-oxidant, anti-microbial and cytotoxic studies, New J. Chem. 41 (18) (2017) 10324–10338.
[37] K.O. Ali, H.M. Ali, T. Gerber, E. Hosten, Mixed Ligand, Palladium (II) and Platinum (II) complexes of tertiary DiphosphineswithS-1H Benzo [d] Imidazole-2-yl Benzothioate, Orient. J. Chem. 33 (2) (2017) 584–592.
[38] A.M.F. Benial, V. Ramakrishnan, R. Murugesan, Infrared and laser Raman studies of [Ni (II)(dppe) Cl2] and [Co (III)(dppe) 2Cl2] PF6 (dppe= 1, 2-bis (diphenylphosphino) ethane), Spectrochim. Acta A Mol. Biomol. Spectrosc. 58 (8) (2002) 1703–1712.
[39] W. Villarreal, et al., Chiral platinum (II) complexes featuring phosphine and chloroquine ligands as cytotoxic and monofunctional DNA-binding agents, Inorg. Chem. 54 (24) (2015) 11709–11720.
[40] T.D. de Oliveira, A.M. Plutín, L. Luna-Dulcey, E.E. Castellano, M.R. Cominetti, A. A. Batista, Cytotoxicity of ruthenium-N, N-disubstituted-N′-acylthioureas complexes, Mater. Sci. Eng. C 115 (2020) 111106.
[41] M.C. Risi, G.C. Saunders, W. Henderson, The coordination chemistry of sulfonyl-substituted thioureas towards the d8 metal centres platinum (II), palladium (II), nickel (II) and gold (III), Inorg. Chim. Acta 526 (2021) 120506.
[42] F.V. Rocha, et al., Synthesis, characterization, X-ray structure, DNA cleavage, and cytotoxic activities of Palladium (II) complexes of 4-Phenyl-3-thiosemicarbazide and Triphenylphosphane, Eur. J. Inorg. Chem. 2013 (25) (2013) 4499–4505.
[43] M.A. Lima, et al., Enhanced anticancer potential of Pd (II)-Thiosemicarbazone complexes: selectivity, mechanisms, and 3D models, Pharmaceutics 17 (7) (2025) 829.
[44] X.-G. Bai, Y. Zheng, J. Qi, Advances in thiosemicarbazone metal complexes as anti-lung cancer agents, Front. Pharmacol. 13 (2022) 1018951.
[45] A. Munshi, M. Hobbs, R.E. Meyn, Clonogenic cell survival assay, in: Chemosensitivity: Volume 1 in Vitro Assays, 2005, pp. 21–28.
[46] N. Brix, D. Samaga, C. Belka, H. Zitzelsberger, K. Lauber, Analysis of clonogenic growth in vitro, Nat. Protoc. 16 (11) (2021) 4963–4991.
[47] G.P. Way, et al., Predicting cell health phenotypes using image-based morphology profiling, Mol. Biol. Cell 32 (9) (2021) 995–1005.
[48] S.K. Koester, W.E. Bolton, Differentiation and Assessment of Cell Death, 1999.
[49] A. Saraste, K. Pulkki, Morphologic and biochemical hallmarks of apoptosis, Cardiovasc. Res. 45 (3) (2000) 528–537.
[50] S. Rello, et al., Morphological criteria to distinguish cell death induced by apoptotic and necrotic treatments, Apoptosis 10 (2005) 201–208.
[51] F. Doonan, T.G. Cotter, Morphological assessment of apoptosis, Methods 44 (3) (2008) 200–204.
[52] G. Banfalvi, Methods to detect apoptotic cell death, Apoptosis 22 (2) (2017) 306–323.
[53] I. Garzón, et al., Evaluation of the cell viability of human Wharton's jelly stem cells for use in cell therapy, Tissue Eng. Part C Methods 18 (6) (2012) 408–419.
[54] Á. Sena-Lopes, et al., Cell viability analysis of Toxocara cati larvae with LIVE/DEAD® Viability/Cytotoxicity kit, Exp. Parasitol. 212 (2020) 107871.
[55] P.S. Steeg, Targeting metastasis, Nat. Rev. Cancer 16 (4) (2016) 201–218.
[56] C.L. Chaffer, R.A. Weinberg, A perspective on cancer cell metastasis, Science (1979) 331 (6024) (2011) 1559–1564.
[57] H.K. Matthews, C. Bertoli, R.A.M. de Bruin, Cell cycle control in cancer, Nat. Rev. Mol. Cell Biol. 23 (1) (2022) 74–88.
[58] G.H. Williams, K. Stoeber, The cell cycle and cancer, J. Pathol. 226 (2) (2012) 352–364.
[59] N.F. Maroufi, et al., Sensitization of MDA-MBA231 breast cancer cell to docetaxel by myricetin loaded into biocompatible lipid nanoparticles via sub-G1 cell cycle arrest mechanism, Naunyn Schmiedeberg's Arch. Pharmacol. 393 (2020) 1–11.
[60] M.S. D'arcy, Cell death: a review of the major forms of apoptosis, necrosis and autophagy, Cell Biol. Int. 43 (6) (2019) 582–592.
[61] N. Kim-Campbell, H. Gomez, H. Bayir, Cell death pathways: apoptosis and regulated necrosis, in: Critical Care Nephrology, Elsevier, 2019, pp. 113–121.
[62] D.V. Krysko, T. Vanden Berghe, K. D'Herde, P. Vandenabeele, Apoptosis and necrosis: detection, discrimination and phagocytosis, Methods 44 (3) (2008) 205–221.